Tsunami inundation and vulnerability analysis at the Makran Coast, Pakistan

Rashid Haider[1,3], Sajid Ali[1], Gösta Hoffmann [2], Klaus Reicherter[1]

[1] Institute of Neotectonics and Natural Hazards, RWTH Aachen University, Lochnerstr. 4-20, 52056 Aachen, Germany
[2] UNESCO Global Geoparks Unit, Department Heritage, Nature, Society, German Commission for UNESCO, Martin-Luther-Allee 42 53175 Bonn, Germany
[3] Geoscience Advanced Research Laboratories, Geological Survey of Pakistan, Islamabad 45500, Pakistan

Correspondence to: Rashid Haider (r.haider@nug.rwth-aachen.de)

Abstract. The coastal cities of Gwadar and Pasni, situated along the Arabian Sea in the northwestern region of the Indian Ocean, are subjected to thorough investigation for inundation and vulnerability analysis. The estimation of maximum tsunami wave potential in the Arabian Sea involves evaluating paleo-morphodynamics records of tsunamites found along its coastlines, with a focus on the most severe case for modeling to determine the maximum wave potential. Subsequently, based on this assessment, three distinct wave scenarios (7 m, 10 m, and 15 m) are projected onto Pasni and Gwadar and their surrounding coastal areas. The results reveal high vulnerability of both cities to wave heights ≥7 m and wave lengths ≥ 15 km, with the 15 m scenario posing a near-complete disaster for both cities and adjoining towns. Furthermore, simulation results demonstrate that the coastal orientation and morphology contribute to the devastating impact of reflection, integration, and amplification phenomena in the region, with their intensity escalating with larger approaching waveforms. The reflection-amplification phenomenon notably and variably impacts inundation extents and depths. The installed tsunami early warning system's effectiveness is also evaluated based on the modeling and simulated results and the recent practices of early warning alerts.

Key words: Arabian Sea tsunami potential, Modelling paleotsunami deposits, Coastal tsunami vulnerability assessment, Makran Subduction Zone

1 Introduction

Tsunamis are rare events but have high damage potential for the coastal communities. Over the past 27 years, 64 tsunamis with a run-up higher than 3 m have been documented globally (Tarbotton et al., 2015). In the recent two decades, there has been a substantial advancement in understanding of tsunami generation, propagation, and inundation. This progress has enabled planners, administrators, and engineers to calibrate building design codes to mitigate disaster risk (Park et al., 2013; Macintosh, 2013). In this context, inundation analysis plays a crucial role in vulnerability and risk assessment. The assessment involves integrating infrastructure fragility curves (damage probability curves) with various tsunami flow magnitudes (Rehman and Cho, 2016). These fragility curves are generated using various techniques based on deterministic

and probabilistic approaches, while tsunami flow magnitude is determined by calculating flow depth and flow velocity through dynamic inundation modeling.

In this paper, two aspects have been investigated: primarily the inundation analysis and secondarily a vulnerability estimation for the coastal cities of Pasni and Gwadar and surrounding areas. These cities were severely affected by the 1945 earthquake (Mw 8.1) entailing tsunami (~12m at Pasni) which resulted in hundreds of casualties (Pendse, 1946; Hoffmann et al., 2013b). In 2013, a small tsunami (<1m) associated with an earthquake (Mw 7.7) struck the same area once more but caused no damage (Heidarzadeh and Satake, 2014b). Both cities had grown many times as compared to those in 1945, and in the event of a similar disaster, substantial loss of life and property is anticipated.

2 Tectonic settings and Associated Seismicity

The majority (80%) of tsunamis globally are triggered by underwater earthquakes (Harbitz et al., 2014; Løvholt, 2017) , while the remaining 20% are caused by other sources such as landslides, volcanoes, and meteoric impacts in the ocean water (Behrens et al., 2021). In the Arabian Sea, seismic activity is primarily attributed to the Makran Subduction Zone (MSZ) (see Fig. 1). The MSZ accommodates the crustal shortening between the Arabian Plate in the south and the Eurasian Plate in the north, converging at a rate of 0.5–20 mm/year (Vernant et al., 2004; Khan et al., 2008; Jade et al., 2017). Most of the seismicity along the eastern MSZ, south of Pasni, is associated with the Sonne Fault (Kukowski et al., 2000). Additionally, the high seismic velocities (4.4 km/s) indicate a brittle decollement at the MSZ, contributing to high seismicity (Smith et al., 2012). This brittle nature is attributed to the lack of soft sediments along the decollement in comparison to the western portion of the MSZ. Thermal modeling of the MSZ suggests a potential earthquake magnitude comparable to the December 2004 Sumatra rupture, possibly reaching up to Mw 9.2 (Smith et al., 2012). Estimates from another thermal modelling research estimates a potential magnitude of Mw 8.65 ± 0.26 in western Makran (Iran) and 8.75 ± 0.26 in eastern Makran, Pakistan (Khaledzadeh and Ghods, 2022). El-Hussain et al. (2016) inversely calculated the maximum moment of earthquake as Mw 8.8 using the geodetic slip rate based on a simplified relation by Brune (1968), Hanks and Kanamori (1979).

The focal mechanism of the 1945 tsunamigenic earthquake indicates a thrust event (Byrne et al., 1992). Dislocation models, body waveform inversion, and moment estimations suggest ruptured lengths ranging from 100 to 200 km, with an average crustal slip of 7 m along the MSZ. The Arabian Plate, while subducting its northern edge, also slides past the Indian Plate in the east at a rate of about 3±1 mm/yr (Reilinger et al., 2006; Rodriguez et al., 2011) making an active transform plate boundary. Murray Ridge (MR) and Owen Fracture Zone (OFZ) are two major tectonic features along this transform plate boundary. The former is a pull apart basin while the latter is a transform boundary (Fig. 1). Minor earthquakes, resulting from right-lateral strike-slip and normal faulting occur in the Murray Ridge (Banghar and Syke, 1981). Seismic activity along the remaining OFZ is mild to moderate, with the largest observed magnitude being Mw 5.8 (Rodriguez et al., 2011), posing no significant tsunami threat.

3 Methods

3.1. Tsunami Wave Potential Assessment

The potential for tsunami waves in the Arabian Sea is also assessed by utilizing the tsunamites proxy. We compiled the reported tsunamites cases around the Arabian Sea and specifically examined the case at Fins, Oman exhibiting extreme morpho-dynamics (Table S1 in supplements). At Fins, the tsunamites are represented by block and boulder deposits up to 40 tonnes lying at a maximum height of 10 m from the mean sea level (msl) showing a landward transportation upto 50 m from their intact sites. Further, laboratory tests on a scaled model (t-LiDAR) of the largest block estimated wave velocities for dislodging, elevating, and transporting these boulders to be between 4.5 to 6.6 meters per second (Hoffmann et al., 2013a). The marine shells (C^{14}, n=4), attached to these blocks and boulders gave a wide range of age between 250±160 and 4595±185 cal. BP (Hoffmann et al., 2020). At the same site, loose tsunami sediments fining and wedging landward with a minimum elevation of ≥17 m is dated 5840 cal. BP (C^{14}, n=6) (Koster et al., 2014). These studies also applied corrections for tectonic uplift/subsidence, absolute sea level change and estimated a 14 m wave run-up. The long-axis rose plot of blocks and boulders indicates that the wave source azimuth (N30E) originates from the MSZ (Hoffmann et al., 2013a). We modelled this case study (Fins Scenario) to estimate the wave size capable of demonstrating the above dynamics. The tsunamis are generated using Okada's (1985) earthquake parameters at MSZ given in Table 1. The other tsunami sources such as landslides, volcanoes, and meteoric impacts in the ocean water have not yet been considered and therefore cannot be negated at this stage.

The 1945 tsunami at Pasni is also a severe event in the known history of tsunamis in the Arabian Sea with reported wave height of 12 m - 15 m (Pendse, 1946). The 1945 tsunami event at Pasni and case of tsunamites at Fins serves as a reference, providing empirical evidence of tsunami potential and its impacts within the region. The recurrence interval for a tsunami event of such magnitude (≥ 10 m) estimated through multiproxy analysis is between 500 to 1000 years (Haider et al., 2023). Based on the above assessment, we establish a range of scenarios (7 m, 10 m, and 15 m) to thoroughly assess the vulnerability landscape of Gwadar and Pasni cities and their surrounding areas.

3.2. Source Type and Parameters

Tsunami propagation and inundation scenarios are modeled using the earthquake parameters on hypothetical splay fault close to the MSZ. We applied Okada's (1985) mathematical model to estimate the seabed deformation induced by earthquakes, employing uniform parameters for a four-segmented fault rupture. The most severe source parameters were replicated based on those investigated in the Fins scenario. To enhance vulnerability assessment, we conducted two additional case studies with scenarios featuring relatively low intensity parameters (Table 1). These scenarios are likely to encompass varying degrees of seismic hazard and tsunami risk, thereby facilitating a more comprehensive evaluation of potential impacts and the formulation of effective mitigation strategies. The relationship between earthquake magnitude and its associated parameters is inherently intricate, primarily owing to the complex geological processes such as fault geometry, heterogeneous stress distribution, and uncertainties in earthquake rupture mechanisms (Zaccagnino et al., 2022). As already

mentioned, the analysis suggests a return period between 500-1000 years for a tsunami ≥ 10 m in the Arabian Sea (Haider et al., 2023). This minimum recurrence interval of 500 years (475 in actuality) correspond to the life safety and infrastructural collapse performance levels (Ahmed et al., 2019). In total three different scenarios have been modelled for enhanced vulnerability assessment of the study area

3.3. Tsunami Modelling and Data Sets

Numerical modelling is performed using the Delft3D 4.04.01 software, developed by the Dutch Institute Deltares (Deltares, 2023). The hydrodynamic programme module Delft3D-FLOW is used for simulation, which solves non-linear 2D and 3D shallow water equations (SWE) for unsteady flow phenomena. The equations of the Boussinesq approximation for incompressible fluids are derived from the three-dimensional hydrodynamic Navier-Stokes equations (for further details, please see ((Deltares, 2023; 168–186). We employed a nested computational grid for both cities, with a grid resolution of 0.0004×0.0004 (44 m × 44 m) for the nested models and 0.01 × 0.01 (~1 km × 1 km) for the regional model. A schematic of the nesting model is provided in Supplements (Simulations-10). In the regional model, Reinmann Boundary Conditions are utilized to minimize the reflection effect, and time-series boundaries are applied for the nested models. For tsunami propagation and inundation analysis, we integrated bathymetric data from the General Bathymetric Chart of the Oceans (GEBCO) at 15 arc seconds resolution and topographic data from the German Aerospace Centre's (DLR) at 0.4 arcsec (~12 m) resolution in a GIS environment. The DLR's topography Digital Elevation Model (DEM) is derived from bistatic X-Band interferometric Synthetic Aperture Radar (SAR) data, utilizing the patented TanDEM-X and TerraSAR-X systems. The post-data acquisition developments, including the addition of the East Bay Express Way and jetty (each 4 meters high), are manually incorporated in the fused DEM, which is particularly crucial for Gwadar. Furthermore, the terrain roughness is assigned using Manning's Coefficient with values ranging as 0.015 sea floor and open land, 0.03 thinly populated areas, 0.05 moderately populated areas to 0.08 densely populated areas. The coefficient value assignment is based on fieldwork, photographs, and Google Earth Satellite Images. The GIS data is analyzed and processed using Quantum Geographical Information System (QGIS 3.28.1) software, providing a robust environment for spatial analysis and visualization. QGIS is an official project of the Open-Source Geospatial Foundation (OSGeo).

3.4. Vulnerability analysis

Damage probability refers to the likelihood or probability of damage that a particular type of property will sustain because of tsunami impact. The vulnerability analysis is carried with the fragility curves expressed as damage probabilities verse drag force of individual houses/structures for structural damage developed by Koshimura et al. (2009) and Rehman and Cho (2016). They computed fragility curves for tsunami damage though statistical approach synergised by GIS/ numerical modelling results of pre/post-tsunami (2004 Indian Ocean Tsunami) data from Banda Aceh, Indonesia. These curves are developed for low-rise, lightly reinforced, non-engineered reinforced concrete (RC) (see Fig. 4). The major structural types in our study area and the Banda Aceh, Indonesia are comparable; mostly single-double story structures with conventional

masonry and lightly engineered RC. The assessment of structural and building material types in the Gwadar and Pasni are based on visual estimates carried out during the field work and need to be worked on in detail for improved results.

In the Koshimura et al. (2009) fragility curves calculated for Banda Aceh, Indonesia, the drag force (hydrodynamic) per unit width of a structure is mathematically expressed as follows:

$$F = \frac{1}{2} C_D \rho u^2 D$$

where C_D is the drag coefficient equal to 0.99 (1.0 for simplicity) and it mainly depends on the shape of the structure and the angle of incidence of the floodwater flow as buildings in our case, ρ is water density (1,000 kg-m^{-3}), u is the wave velocity (ms^{-1}), and D the inundation/ flow depth (m). The drag force for each scenario is calculated using this hydrodynamics at each monitoring point in Gwadar and Pasni. For example, in Pasni, the drag force (*F*) for 15 m Scenario at Monitoring Point (M2) is calculated using the modelled flow depth/velocity as:

$$F = \frac{1}{2}(1)(1000)(2)^2(8)$$

$$F = 16{,}000\ Nm$$

$$F = 16\ kNm$$

4 Results and Interpretations

4.1. Pasni scenarios

In the 7 m scenario, the first wave reaches the Pasni coast in 20 minutes after the earthquake. From coastline (shoreline) it further takes 20 minutes to reach its maximum inundation limit, partly affecting localities of Wadsar and Main Bazar. In this inundation course, only one monitoring point (M5) situated in inhabited locality experiences inundation. The M5 records a maximum flow depth of 1 meter and flow velocity of 0.5 m/s. However, areas like Shol, Parhag, and a significant part of the main Pasni town remain relatively unaffected (see Fig. 2; 7m scenario).

In the 10 m scenario, along with first wave a secondary wave with a height of 8 m is generated due to reflection from the cliffs northeast of Pasni (Supplements: Simulations-3 Pasni 10 m scenario). These two waveforms reach the Pasni coast at intervals of 20 minutes and 45 minutes, respectively, following the earthquake (see Fig. 2 M6: 10 m scenario). In both cases, the inundation pattern shifts based on wave propagation direction: initially, northward propagation inundates the southeast of area, while southward propagation due to reflection causes inundation from the northeast. Initially, the approaching wave inundates the study area from south and inundation extent decreases significantly northward, primarily due to the adjacent river (Shadi Kaur) consuming a significant portion of the inundating wave, resulting in lower water levels in the populated area. Nonetheless, the inundation dynamics pose a significant threat to loss of life and property. Spatially, the inundation gradually decreases from south to north, with maximum flow depth and flow velocity at M1 being 6 m and 2.5 ms^{-1}, to 2 m and 1 ms^{-1} at M6.

In the 15 m scenario, the inundation impact is approximately double in terms of flow depth as compared to that in the 10 m scenario due to the heightened wave characteristics and enhanced reflection phenomenon. The approaching and reflecting waves interact for a duration of 30 minutes, generating a series of wavelets that gradually increase in intensity and contributing to the formation of a larger and more complex waveform. Consequently, a significant accumulation of water along the shoreline in the study area results in far and deeper inundation (Supplements: Simulations-4 Pasni 15 m scenario). The flow velocity spectral characteristics exhibit a higher degree of complexity and variability in comparison to the corresponding flow depth. In populated areas, such as Pasni, Main Bazar, Parhag, and Wadsar, peak flow depths range between 6 to 8 meters, alongside maximum flow velocities reaching 1.5 ms^{-1}. The intense backwash process in this scenario poses a significant hazard too, as evidenced by the consistent recording of flow depths exceeding 1 meter at all monitoring points until the 5-hour simulation duration (see Fig. 2 M6: 15m scenario).

In general, for all three scenarios, the maximum flow velocity is recorded through the first wave and maximum flow depth is recorded at quasi-still stand. Quasi-still stand refers to temporary pause or halt at maximum inundation limit after which the backwash process initiates. The backwash tsunami phenomenon persists for more than 4 hours.

4.2. Gwadar scenarios

The East Gwadar Bay or simply the east bay is characterized by two prominent coastal wave reflectors; one to the north as coastal mountains namely Mehdi-Koh and other to the south as Gwadar-Hammer-Head (see Fig. 3). The Gwadar-Hammer-Head is a geological formation characterized by a protruding landmass extending into the sea. The subsequent reflection phenomena and the ingress of regular tsunami waves (≤ 4m) contribute to wave integration and amplification along with delayed wave arrivals. For instance, in the 7 m scenario at M1 (Mohalla Band locality), the first wave arrives 30 minutes after the earthquake, with a flow depth of 1 m. Further, with a lapse of 15 minutes, the second wave inundates the area increasing the flow depth to 2.6 m. This is succeeded by a third wave after a lapse of an additional 30 minutes further increasing the flow depth to 3 m. After the third and final wave the quasi still stand or a temporary water stabilization prevails for 15 minutes. Hence, with the reflection mechanism in place, the water level exhibits a continuous increase over a span of 60 minutes. However, if we eliminate the influence of reflection from the first tsunami wave, this duration would be reduced to merely 15 minutes with only 1 m flow depth at M1. The wave spectral analysis shows an inverse relation of flow depth and flow velocity because of the loss of kinetic energy during reflection-amplification phenomenon.

The Surbandar locality (M4) remains unaffected in the 7 m scenario, however in 10 m and 15 m scenarios the locality is severely affected. It is positioned at a lower elevation compared to the beach banks in the south from where the tsunami propagates and experiences wave overflow. Being situated on low-lying topography as compared to the beach banks and by the direct facing to the tsunami, the torrential force achieves a flow velocity of 4 ms^{-1} and 6 ms^{-1} in 10 m scenario and 15 m scenario, respectively. Similar phenomenon is observed for Pishukan locality (M5) also. The cliffs, averaging a height of 12 meters, situated to the south of Pishkun provide protection against inundation in scenarios of 7 m and 10 m. However, in the 15 m scenario, waves spill over these natural defenses, resulting in flow depths and velocities of 3 m and 2.1 ms^{-1}

respectively at M5. The New Town locality (M2) exhibits the highest flow depth in each scenario, reflecting its heightened vulnerability to tsunami inundation. Analysis reveals that this high vulnerability arises from inundation originating from both the east and west bays, where wave interactions lead to amplification of the inundating waves.

In the Gwadar town (M1 to M2), both sides of the bay are elevated to a height of 5 meters above mean sea level (MSL) to accommodate road construction. This elevated terrain, coupled with an inadequate and low-capacity drainage infrastructure, significantly impedes the backwash process of tsunamis (see Fig. 3 flow depths: all scenarios). Modeling results indicate a flow depth exceeding 2 m in the Gwadar town even after three hours.

4.3. Vulnerability Analysis

The damage probability for each scenario is assessed through hydrodynamic analysis conducted at each monitoring point in both cities. Consequently, damage intensity is expected to escalate towards the shoreline from these monitoring locations. However, exceptions are noted in the cases of the Surbandar and Pishukan in Gwadar area, which are elaborated later.

At Pasni, monitoring points M1 and M2 exhibit the most severe flow dynamics, indicating the highest vulnerability to tsunami inundation in each scenario (see Fig. 4; Pasni scenarios). For M1, the damage probabilities are 0.50, 0.95, and 1.0 for the 7 m, 10 m, and 15 m scenarios, respectively. Similarly, for M2, the corresponding probabilities are 0.05, 0.6, and 0.95. Despite being uninhabited, any development should undergo feasibility studies concerning extreme wave events, particularly tsunamis. Regarding the inhabited part, the 7 m scenario minorly affects the Main Bazar locality (M5) and surrounding areas with an estimated damage probability close to zero. However, it should be noted that infrastructure or communities residing in close proximity to the shoreline may still possess some degree of damage potential. In the 10 m scenario, the Wadsar locality (M3) poses the maximum damage potential with probability of 0.57, followed by Main Bazar (M5) with 0.37, and then Pasni locality (M6) with 0.05. In the 15 m scenario, no locality remains unaffected; all localities exhibit a probability of damage exceeding 0.6, except for Shol (M7), which registers a value of 0.4.

The results indicate that the level of vulnerability and probability of damage are higher in the Gwadar area compared to the Pasni area. In the 7 m scenario, three localities, two of which are inhabited, are inundated (see Fig. 4; Gwadar scenarios). The Mohalla Band locality (M1) exhibits a damage probability of 0.4, followed by the New Town locality (M2) with 0.1. Additionally, the proposed site for industrial development (M3) is also inundated, with a damage probability of less than 0.1. The 10 m and 15 m scenarios pose significant challenges for the area. In the 10 m scenario, only Pishukan remains unimpacted, while all other localities are anticipated to experience a damage probability exceeding 0.8. The findings indicate that the Surbandar locality (M4) encounters a hydrodynamic force exceeding 40 kNm. This heightened level is attributed to tsunami overtopping the beach banks followed by a torrential downslope runoff effect, as discussed earlier in the section (section 4.2.). All localities, except Pishukan, have a damage probability of 1.0, with hydrodynamic force exceeding 35 kNm. The Pishukan locality (M5) indicates a probability of 0.6 in case of a 15 m tsunami only.

5 Discussion and Conclusions

The process of tsunami modeling comprises three distinct phases: generation, propagation, and inundation. The generation phase involves calculation of sea floor deformation during an earthquake causing initial disturbance in the oceanic water. Subsequently, a hydrodynamic model utilizes this initial wave to model and simulate the propagation and inundation of the tsunami waves. For tsunami generation and potential estimation, utilizing Okada's (1985) model for the initial sea floor deformation is a valuable asset in seismic and tsunami hazard assessment. However, it is imperative to refer to the model's inherent limitations and their potential impact on our findings. Primarily, the model's static nature and its reliance on a single linear fault plane geometry, coupled with its exclusion of material properties considerations, pose notable constraints. These constraints may result in an underestimation or overestimation of tsunami hazard levels, emphasizing the need for caution and further investigation when interpreting our results. To have better results for generation and potential estimation, we compiled and analyzed the tsunamites discovered along the Arabian Sea shorelines and took the case exhibiting worse morphodynamics for modeling purposes. Subsequently, utilizing Okada's (1985) fault parameters, various tsunami wave scenarios are generated along the MSZ to find the capable one aligning with both field and laboratory readings of tsunamites case taken up. As a result, our study provides a better waves tsunami potential estimation and an indirect approximation of potential fault parameters and earthquake potential, offering valuable insights into tsunami hazard assessment.

In tsunami hazard assessment, wave height is considered a yardstick, while wavelength tends to be overlooked. We assessed that for vulnerability and risk assessment, along with wave height, the wavelength must be taken into consideration. To illustrate this point, we conducted simulations involving two scenarios with identical wave heights of 5 m but differing wavelengths ($\lambda/2$) of 15 km and 3 km, impacting the Pasni coast (see Supplements: Simulations-9). The wave with the shorter wavelength dissipated faster without causing any inundation, whereas the longer wavelength resulted in considerable inundation, with a runup height of 2 m and an inundation extent of 0.7 km. This disparity can be attributed to a smaller quantity of displaced water and wave dispersion phenomenon that disperses rapidly and diminishes in magnitude during propagation, confining the hazards to local areas only. Vertical seafloor deformation or coseismic displacement tends to result in tsunamis characterized by longer wavelengths and longer periods when compared to those generated by landslide failures, mainly because of the broader source area associated with coseismic displacement events (Hammack, 1973; Watts, 1998; Heidarzadeh et al., 2014).

The bare ground elevation model represents a digital topography with no building infrastructure, plants, poles, etc. It is formally known as the digital terrain model (DTM). For inundation analysis, the deflection of DEM from DTM hampers the results in two aspects: i) the porous infrastructure, such as houses, mangroves etc., does not account for water balance adjustments. These features in DEM act as solid bodies, occupying the volume and deflecting the inundating water further ahead, resulting in higher inundation extents. ii) In the case of a low-resolution DEM which could not resolve the streets or passages results in water damming. It consequently, results in higher flow depths downstream than actual, and it also affects the backwash computations. Along with improving the spatial resolution, a water absorption and permeability value may be

incorporated to each feature in the land use map which could accounts for volumetric crossflow though structures adjustment of inundating water.

The effectiveness of the tsunami early warning system is assessed in terms of far-field and near-field sources particularly for the study area. An integrated Indian Ocean Tsunami Early Warning System is developed under the framework of Intergovernmental Oceanographic Commission (IOC-IOTWS) under the UNESCO umbrella in response to the tragic tsunami on 26th December 2004. The near-field tsunami warning is issued based on the location, size and initial evaluation of earthquake fault parameters through seismic spectral signatures. The Pakistan Meteorological Department (PMD) in collaboration with IOC-IOTWS is responsible for keeping track of coastal hazards and issuance of tsunami notifications and alerts. For earthquakes Mw $\geq$ 6.5 in the Arabian Sea, a near-shore early warning system puts the coastal community immediately under alert and watch status until confirmation of tsunami generation. The tsunami confirmation warning is issued once the tsunami wave is detected on any sensor or tide gauge which is either installed at the coast or DART station (Deep-ocean Assessment and Reporting of Tsunamis). In the study areas these gauges are installed at Gwadar and Pasni ports and the nearest DART station 450 km from the MSZ. The numerical models show, the first tsunami wave generated at eastern MSZ arrives at the Pasni Coast (Pasni tide gauge) and the nearest DART in 15 and 45 minutes, respectively. Heidarzadeh et al. (2007) calculated these timings as 15 and 60 minutes, respectively. If the tsunami had generated at eastern MSZ, it would reach the Makran Coast before its instrumental detection and confirmation warning. So, the coastal community will surpass the confirmation warning and therefore had to rely on the advisory (alert and watch) warning only. On the other hand, the confirmation warning system works very well for the far-source tsunamis as a number of gauges installed at eastern Indian Coast, Maldives and DART stations detects the propagating tsunami several hours before reaching the Makran Coast (Srinivasa Kumar and Manneela, 2021). Further, three case studies from the Indian Ocean are presented for assessment of general practices and timelines in terms of detection, warning, and confirmation. The timeline for these chain of events during each tsunami case is given in (Table S2 in supplements).

Since the installation of IOTWS, 2013 Tsunami is the only near-field tsunami generated in the Arabian Sea. It was triggered remotely by a terrestrial earthquake located near the Khuzdar city, Pakistan. The tsunami waves remained almost unnoticed by the community due to the low wave heights and its occurrence at low tide. As it is thought to be triggered by an underwater landslide, the exact trigger time and location are not known. However, through reverse modelling the source position at offshore of the Pakistan is estimated in between Gwadar and MSZ (Hoffmann et al., 2014). Form this tsunami source, the waves would have reached the Gwadar Coast within 5-20 minutes. After the earthquake, the first advisory warning followed by second confirming “no tsunami” warning was issued 11 minutes and 16 minutes, respectively after the earthquake. The advisory warning confirmation was particularly issued on the bases of epicentre being on the terrestrial (inland) part. The tsunami was first detected instrumentally 39 minutes after the earthquake at the Qurayat tide gauge in Oman. Various other tide gauges also recorded the tsunami afterward. The DART detected the tsunami wave 72 minutes after the earthquake. No further warning was issued may be due to small scale of the tsunami. Regarding the far-field tsunami, we analysed two cases: July 17, 2006, Java and October 25, 2010, Mentawai, Indonesia Tsunamis. In both cases,

the system worked very well to warn the far-field communities. However, in both cases the waves arrived at nearest coast of Indonesia before issuance of 1st advisory warning (details in Table S2 in supplements). The tsunami confirmation warnings in both cases were issued 19 minutes after of the earthquake at international early warning system where all local and regional warning systems are connected. These tsunamis took around 8 hours to reach the Makran Coast providing enough time to inform and evacuate the community. Here, we emphasize the importance of alert-watch awareness and preparedness for the communities residing close to tsunami source. In some tsunami cases, natural signs as the receding water after an earthquake and a strong and unusual roar sound may help an early warning for coastal communities. Technically, the initial recording of coastline or the draw down is due to development of initial wave trough along the coast. However, this may not always be the case because the trough development is subjected to source characteristic and position of the tsunami source. The awareness coupled with trainings, route evacuation and to react during such disasters is also very important. The PMD also has a well-established cyclone early warning system operating since 1960s. Despite multiple early warnings issued to coastal communities (couple of days earlier) the high number of fatalities and property losses from the cyclones in 1998, 1999, 2007, 2010, and 2021 demonstrate dismal levels in terms of resilience and preparedness. Likewise, in case of a tsunami the impact appears to be far harsher.

Authors contributions

RH constructed the idea, planned the methodology, interpreted the results, and then reached conclusions. KR supervised the whole process and provided technical, environmental, financial, and personal support for the research work. GH co-supervised the process. SA reviewed the literature.

Data availability

Not applicable

Competing interests

The authors declare that they have no conflict of interest.

Financial support

The research work is generously supported by the German Academic Exchange Service (DAAD) (Research Grants-Doctoral Programme no. 57507871).

Acknowledgement

We are grateful to the German Aerospace Center for providing the unprocessed digital elevation model data (TanDEM-X, DEM 12 m) for the inundation analysis.

References

Ahmed, M., Lodi, S. H. and Rafi, M. M.: Probabilistic seismic hazard analysis based zoning map of Pakistan, J. Earthq. Eng., 1–36, doi:10.1080/13632469.2019.1684401, 2019.

Banghar, A. and Syke, L. R.: Focal mechanism of an earthquake from the Southern Ocean, Tectonophysics, 79, 37–41, 1981.

Behrens, J., Løvholt, F., Jalayer, F., Lorito, S., Salgado-Gálvez, M. A., Sørensen, M., Abadie, S., Aguirre-Ayerbe, I., Aniel-Quiroga, I., Babeyko, A., Baiguera, M., Basili, R., Belliazzi, S., Grezio, A., Johnson, K., Murphy, S., Paris, R., Rafliana, I., De Risi, R., Rossetto, T., Selva, J., Taroni, M., Del Zoppo, M., Armigliato, A., Bureš, V., Cech, P., Cecioni, C., Christodoulides, P., Davies, G., Dias, F., Bayraktar, H. B., González, M., Gritsevich, M., Guillas, S., Harbitz, C. B., Kânoğlu, U., Macías, J., Papadopoulos, G. A., Polet, J., Romano, F., Salamon, A., Scala, A., Stepinac, M., Tappin, D. R., Thio, H. K., Tonini, R., Triantafyllou, I., Ulrich, T., Varini, E., Volpe, M. and Vyhmeister, E.: Probabilistic Tsunami Hazard and Risk Analysis: A Review of Research Gaps, Front. Earth Sci., 9(April), 1–28, doi:10.3389/feart.2021.628772, 2021.

Brune, J. N.: Seismic moment, seismicity, and rate of slip along Major fault zones, J. Geophys. Res., 73(2), 1968.

Byrne, D. E., Sykes, L. R. and Davis, D. M.: Great thrust earthquakes and aseismic slip along the plate boundary of the Makran Subduction Zone, J. Geophys. Res., 97(B1), 449–478 [online] Available from: http://onlinelibrary.wiley.com/doi/10.1029/91JB02165/full, 1992.

Chacón-Barrantes, S., Narayanan, R. R. A. and Mayerle, R.: Several tsunami scenarios at the North Sea and their consequences at the German Bight., 2013.

Deltares: Delft3d-Flow; simulation of multi-dimensional hydrodynamic flows and transport phenomena, including sediments. https://content.oss.deltares.nl/delft3d4/Delft3D-FLOW_User_Manual.pdf, , 1–725, 2023.

El-Hussain, I., Omira, R., Deif, A., Al-Habsi, Z., Al-Rawas, G., Mohamad, A., Al-Jabri, K. and Baptista, M. A.: Probabilistic tsunami hazard assessment along Oman coast from submarine earthquakes in the Makran subduction zone, Arab. J. Geosci., 9(15), doi:10.1007/s12517-016-2687-0, 2016.

Gelfenbaum, G., Vatvani, D., Jaffe, B. and Dekker, F.: Tsunami inundation and sediment transport in vicinity of coastal mangrove forest, Coast. Sediments ’07 - Proc. 6th Int. Symp. Coast. Eng. Sci. Coast. Sediment Process., 1–12, doi:10.1061/40926(239)86, 2007.

Haider, R., Ali, S., Hoffmann, G. and Reicherter, K.: A multi-proxy approach to assess tsunami hazard with a preliminary risk assessment: A case study of the Makran Coast, Pakistan, Mar. Geol., 107032, doi:https://doi.org/10.1016/j.margeo.2023.107032, 2023.

Hammack, J. L.: A note on tsunamis: Their generation and propagation in an ocean of uniform depth, J. Fluid Mech., 60(4),

769–799, doi:10.1017/S0022112073000479, 1973.

Hanks, T. C. and Kanamori, H.: A moment magnitude scale, J. Geophys. Res. B Solid Earth, 84(B5), 2348–2350, doi:10.1029/JB084iB05p02348, 1979.

Harbitz, C. B., Løvholt, F. and Bungum, H.: Submarine landslide tsunamis: How extreme and how likely?, Nat. Hazards, 72(3), 1341–1374, doi:10.1007/s11069-013-0681-3, 2014.

Heidarzadeh, M. and Satake, K.: Possible sources of the tsunami observed in the northwestern Indian ocean following the 2013 September 24 Mw 7.7 Pakistan inland earthquake, Geophys. J. Int., 199(2), 752–766, doi:10.1093/gji/ggu297, 2014.

Heidarzadeh, M., Pirooz, M. D., Zaker, N. H. and Mokhtari, M.: Modeling of tsunami propagation in the vicinity of the southern coasts of Iran, Int. J. Civ. Eng., 5(4), 223–234, doi:10.1115/OMAE2007-29082, 2007.

Heidarzadeh, M., Krastel, S. and Yalciner, A. C.: The state-of-the-art numerical tools for modeling landslide tsunamis: a short review, in Submarine mass movements and their consequences: 6th international symposium, pp. 483–495, Springer., 2014.

Hoffmann, G., Reicherter, K., Wiatr, T., Grützner, C. and Rausch, T.: Block and boulder accumulations along the coastline between Fins and Sur (Sultanate of Oman): Tsunamigenic remains?, Nat. Hazards, 65(1), 851–873, doi:10.1007/s11069-012-0399-7, 2013a.

Hoffmann, G., Rupprechter, M., Balushi, N. Al, Grützner, C. and Reicherter, K.: The impact of the 1945 Makran tsunami along the coastlines of the Arabian Sea (Northern Indian Ocean) – a review, Zeitschrift für Geomorphol. Suppl. Issues, 57(4), 257–277, doi:10.1127/0372-8854/2013/s-00134, 2013b.

Hoffmann, G., Al-Yahyai, S., Naeem, G., Kociok, M. and Grützner, C.: An Indian Ocean tsunami triggered remotely by an onshore earthquake in Balochistan, Pakistan, Geology, 42(10), 883–886, doi:10.1130/G35756.1, 2014.

Hoffmann, G., Grützner, C., Schneider, B., Preusser, F. and Reicherter, K.: Large Holocene tsunamis in the northern Arabian Sea, Mar. Geol., 419(September 2019), doi:10.1016/j.margeo.2019.106068, 2020.

Jade, S., Shrungeshwara, T. S., Kumar, K., Choudhury, P., Dumka, R. K. and Bhu, H.: India plate angular velocity and contemporary deformation rates from continuous GPS measurements from 1996 to 2015, Sci. Rep., 7(1), 1–16, doi:10.1038/s41598-017-11697-w, 2017.

Khaledzadeh, M. and Ghods, A.: Estimation of size of megathrust zone in the Makran subduction system by thermal modelling, Geophys. J. Int., 228(3), 1530–1540, doi:10.1093/gji/ggab417, 2022.

Khan, M. A., Bendick, R., Bhat, M. I., Bilham, R., Kakar, D. M., Khan, S. F., Lodi, S. H., Qazi, M. S., Singh, B., Szeliga, W. and Wahab, A.: Preliminary geodetic constraints on plate boundary deformation on the western edge of the Indian plate from TriGGnet (Tri-University GPS Geodesy Network), J. Himal. Earth Sci., 41(May), 71–87, 2008.

Koshimura, S., Oie, T., Yanagisawa, H. and Imamura, F.: Developing fragility functions for tsunami damage estimation using numerical model and post-tsunami data from banda aceh, Indonesia, Coast. Eng. J., 51(3), 243–273, doi:10.1142/S0578563409002004, 2009.

Koster, B., Hoffmann, G., Grützner, C. and Reicherter, K.: Ground penetrating radar facies of inferred tsunami deposits on

the shores of the Arabian Sea (Northern Indian Ocean), Mar. Geol., 351, 13–24, doi:10.1016/j.margeo.2014.03.002, 2014.

Kukowski, N., Schillhorn, T., Flueh, E. R. and Huhn, K.: Newly identified strike-slip plate boundary in the northeastern Arabian Sea, Geology, 28(4), 355–358, doi:10.1130/0091-7613(2000)28<355:NISPBI>2.0.CO;2, 2000.

Løvholt, F.: Tsunami Hazard and Risk Assessment, United Nations Off. Disaster Risk Reduct., (July), 1–9 [online] Available from: https://www.unisdr.org/we/inform/publications/57441, 2017.

Macintosh, A.: Coastal climate hazards and urban planning : how planning responses can lead to maladaptation, , 1035–1055, doi:10.1007/s11027-012-9406-2, 2013.

Okada, Y.: Surface deformation due to shear and tensile faults in a half space, Bull. - Seismol. Soc. Am., 75(4), 1135–1154, doi:10.1785/bssa0820021018, 1985.

Van Ormondt, M., Nederhoff, K. and Van Dongeren, A.: Delft Dashboard: A quick set-up tool for hydrodynamic models, J. Hydroinformatics, 22(3), 510–527, doi:10.2166/hydro.2020.092, 2020.

Park, S., van de Lindt, J. W., Cox, D. and Gupta, R.: Concept of Community Fragilities for Tsunami Coastal Inundation Studies, Nat. Hazards Rev., 14(4), 220–228, doi:10.1061/(asce)nh.1527-6996.0000092, 2013.

Pendse, C. G.: The Mekran Earthquake of the 28th November 1945, Sci. Notes, X(125), 141–146, 1946.

Rehman, K. and Cho, Y. S.: Building damage assessment using scenario based tsunami numerical analysis and fragility curves, Water (Switzerland), 8(3), doi:10.3390/w8030109, 2016.

Reilinger, R., McClusky, S., Vernant, P., Lawrence, S., Ergintav, S., Cakmak, R., Ozener, H., Kadirov, F., Guliev, I., Stepanyan, R., Nadariya, M., Hahubia, G., Mahmoud, S., Sakr, K., ArRajehi, A., Paradissis, D., Al-Aydrus, A., Prilepin, M., Guseva, T., Evren, E., Dmitrotsa, A., Filikov, S. V., Gomez, F., Al-Ghazzi, R. and Karam, G.: GPS constraints on continental deformation in the Africa-Arabia-Eurasia continental collision zone and implications for the dynamics of plate interactions, J. Geophys. Res. Solid Earth, 111(5), 1–26, doi:10.1029/2005JB004051, 2006.

Röbke, B. R., Schüttrumpf, H. and Vött, A.: Effects of different boundary conditions and palaeotopographies on the onshore response of tsunamis in a numerical model - A case study from western Greece, Cont. Shelf Res., 124(September 2000), 182–199, doi:10.1016/j.csr.2016.04.010, 2016.

Röbke, B. R., Schüttrumpf, H. and Vött, A.: Hydro- and morphodynamic tsunami simulations for the ambrakian gulf (Greece) and comparison with geoscientific field traces, Geophys. J. Int., 213(1), 317–339, doi:10.1093/gji/ggx553, 2018.

Rodriguez, M., Fournier, M., Chamot-Rooke, N., Huchon, P., Bourget, J., Sorbier, M., Zaragosi, S. and Rabaute, A.: Neotectonics of the Owen Fracture Zone (NW Indian Ocean): Structural evolution of an oceanic strike-slip plate boundary, Geochemistry, Geophys. Geosystems, 12(12), doi:10.1029/2011GC003731, 2011.

Smith, G. L., McNeill, L., Henstock, I. J. and Bull, J.: The structure and fault activity of the Makran accretionary prism, J. Geophys. Res., 117(7), 1–17, doi:10.1029/2012JB009312, 2012.

Srinivasa Kumar, T. and Manneela, S.: A Review of the Progress, Challenges and Future Trends in Tsunami Early Warning Systems, J. Geol. Soc. India, 97(12), 1533–1544, doi:10.1007/s12594-021-1910-0, 2021.

Sujatmiko, K. A., Ichii, K., Murata, S. and Mulia, I. E.: Application of Stress Parameter from Liquefaction Analysis on the

Landslide Induced Tsunami Simulation : A Case Study of the 2018 Palu Tsunami, , 18(3), 199–208, doi:10.20965/jdr.2023.p0199, 2023.

Tarbotton, C., Dall'Osso, F., Dominey-Howes, D. and Goff, J.: The use of empirical vulnerability functions to assess the response of buildings to tsunami impact: Comparative review and summary of best practice, Earth-Science Rev., 142, 120–134, doi:https://doi.org/10.1016/j.earscirev.2015.01.002, 2015.

Tran-Cong, S., Gay, M. and Michaelides, E. E.: Drag coefficients of irregularly shaped particles, Powder Technol., 139(1), 21–32, doi:10.1016/j.powtec.2003.10.002, 2004.

Vernant, P., Nilforoushan, F., Hatzfeld, D., Abbassi, M. R., Vigny, C., Masson, F., Nankali, H., Martinod, J., Ashtiani, A., Bayer, R., Tavakoli, F. and Chéry, J.: Present-day crustal deformation and plate kinematics in the Middle East constrained by GPS measurements in Iran and northern Oman, Geophys. J. Int., 157(1), 381–398, doi:10.1111/j.1365-246X.2004.02222.x, 2004.

Wadell, H.: The coefficient of resistance as a function of Reynolds number for solids of various shapes, J. Franklin Inst., 217(4), 459–490, doi:https://doi.org/10.1016/S0016-0032(34)90508-1, 1934.

Watts, P.: Wavemaker Curves for Tsunamis Generated by Underwater Landslides, J. Waterw. Port, Coastal, Ocean Eng., 124(3), 127–137, doi:10.1061/(asce)0733-950x(1998)124:3(127), 1998.

Zaccagnino, D., Telesca, L. and Doglioni, C.: Scaling properties of seismicity and faulting, Earth Planet. Sci. Lett., 584(March), 117511, doi:10.1016/j.epsl.2022.117511, 2022.

Figures and tables

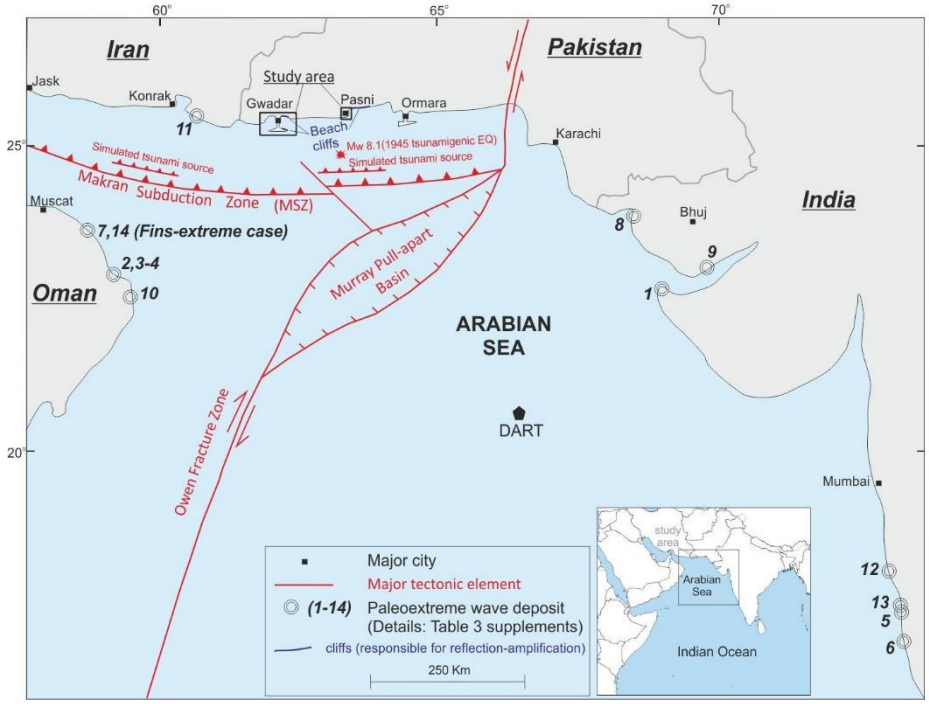

Figure 1: A Location and tectonic map of the study areas (Gwadar, Pasni). The circles with numbers show the reported palaeoextreme wave deposits; details are in Table S1 in the supplements. DART: Deep-ocean Assessment and Reporting of Tsunamis.

Table 1: Table showing the earthquake source parameters used to model each scenario with respective initial wave height.

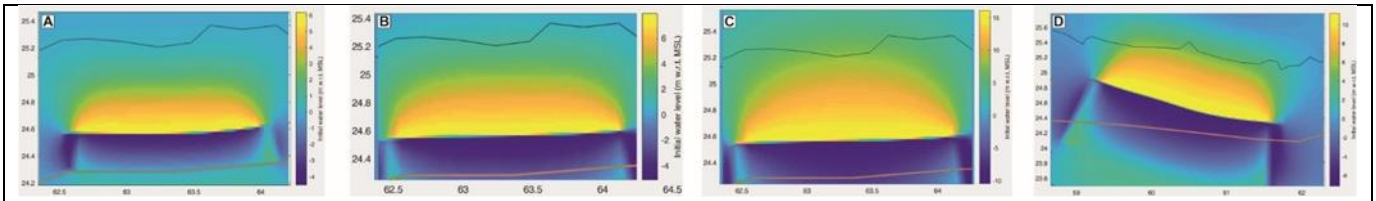

Initial Wave height		Length (km)	Strike (deg)	Width (km)	Depth (km)	Dip (deg)	Rake (deg)	Slip (m)
A)7m Scenario	East MSZ	200	266 to 269	110	10	35	90	8
B)10m Scenario		200	266 to 269	160	10	35	90	10
C)15m Scenario		200	266 to 269	211	10	35	90	22
D)Fins Scenario (15m)		200	-84 to -70	211	10	35	90	22
D represents the initial wave height generated for modeling the Fins Tsunamites case. A, B, and C represent the initial wave heights for the Pasni and Gwadar areas.								

Table 2: Summarized methodology with flowchart showing sequential order of various processes used for hazard and vulnerability assessment.

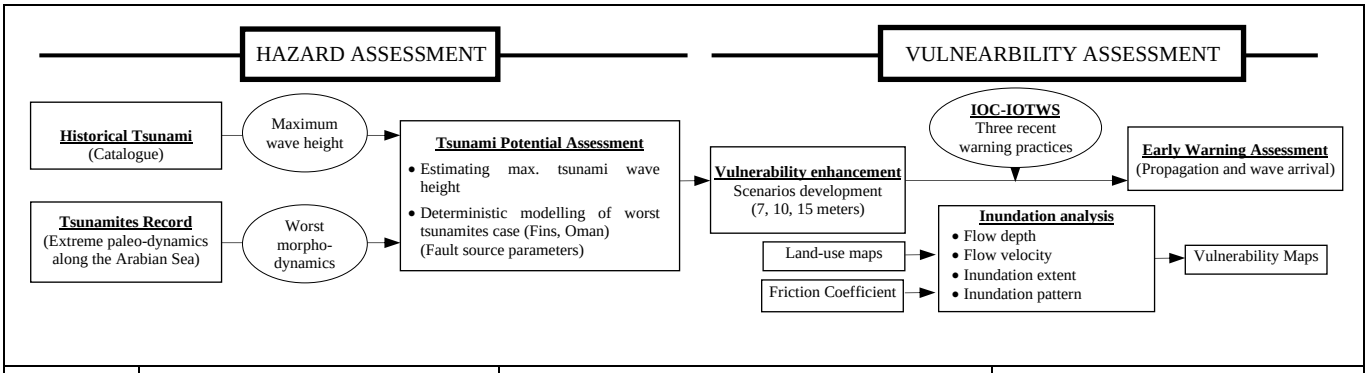

Approach	Model	Equation/s	Reference
Hydrodynamic	**Delft3D (Flow module, Dashboard)** • mass conservation • momentum eq. • surface roughness • simulations	• *Hydrodynamic equations* • *Continuity equation* • *Momentum equations in horizontal direction* • *Vertical velocities* • *Hydrostatic pressure assumption* • *Coriolis force and Reynolds stresses equations* * For details, referred to (Deltares, 2023), pp. 168–186)	(Deltares, 2023) (Gelfenbaum et al., 2007) (Chacón-Barrantes et al., 2013) (Röbke et al., 2016) (Röbke et al., 2018) (Van Ormondt et al., 2020) (Sujatmiko et al., 2023)

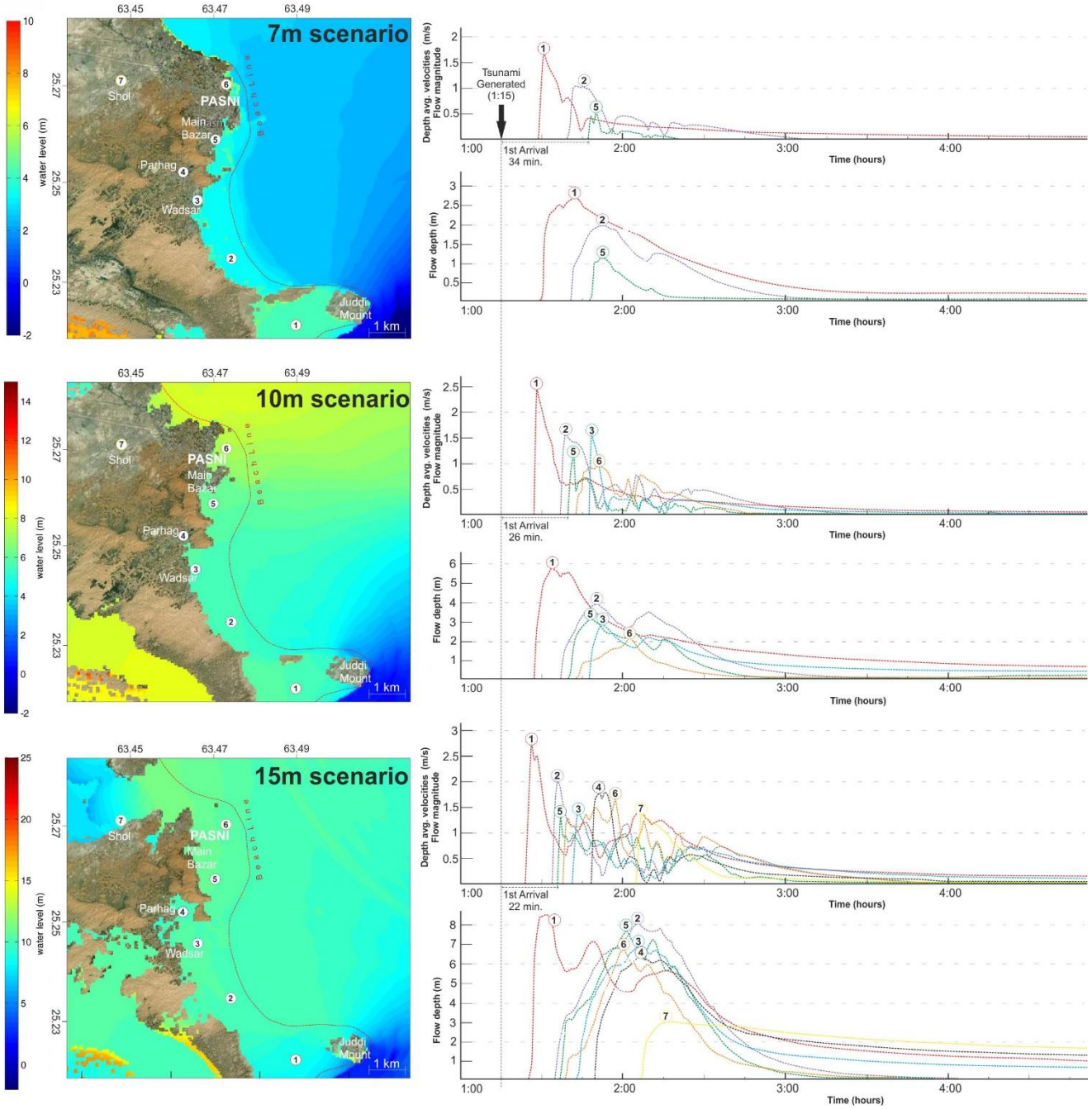

Figure 2: Hydrodynamic modelling results of each scenario with maximum inundation limits and depths at Pasni and surrounding areas. The graphs illustrate the flow depth and magnitude at monitoring points (M1 to M7). Simulation details for each scenario are provided in the supplementary materials.

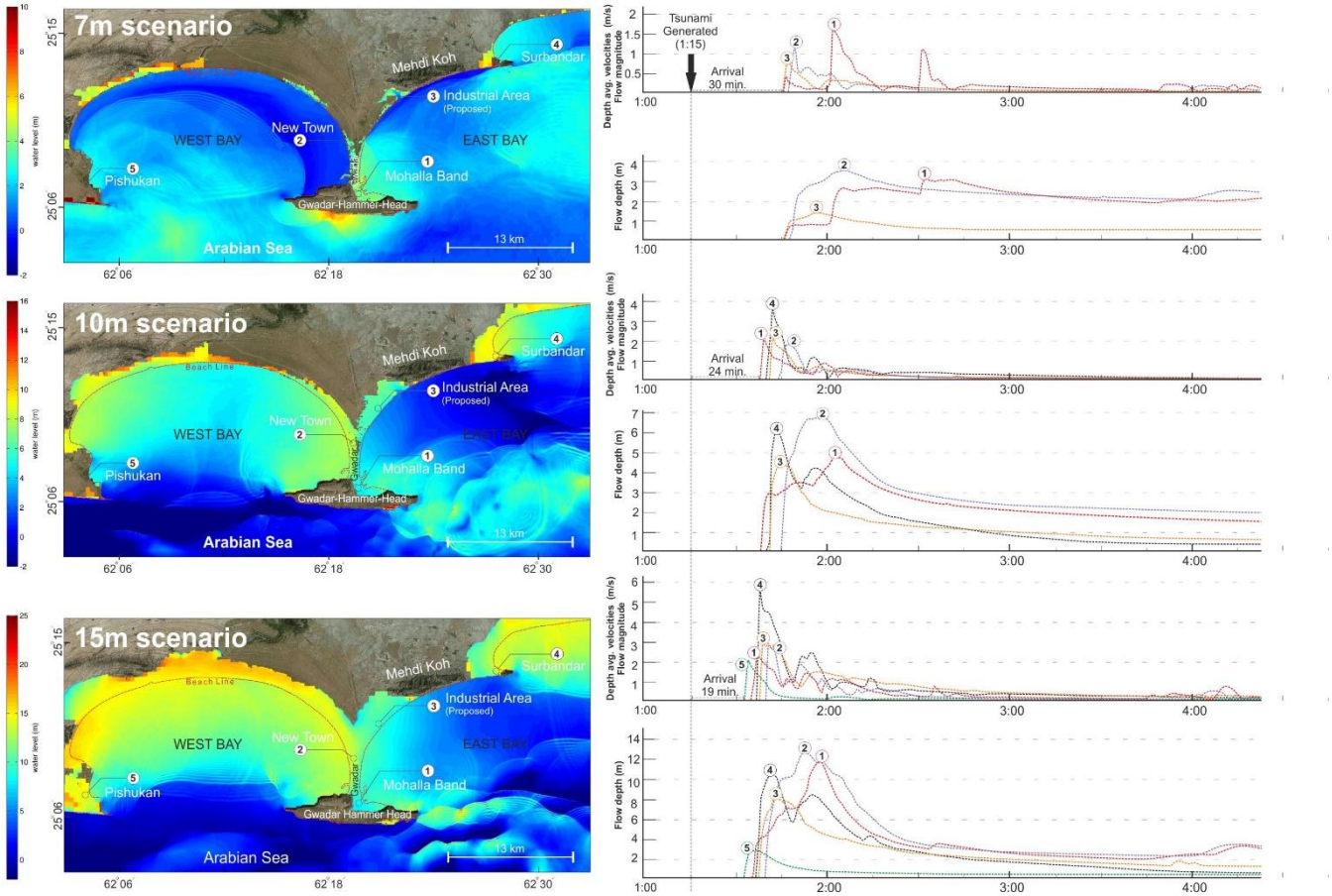

455 **Figure 3: Hydrodynamic modelling results of each scenario with maximum inundation limits and depths at Gwadar and surrounding areas. The graphs illustrate the flow depth and magnitude at monitoring points (M1 to M5). Simulation details for each scenario are provided in the supplementary materials.**

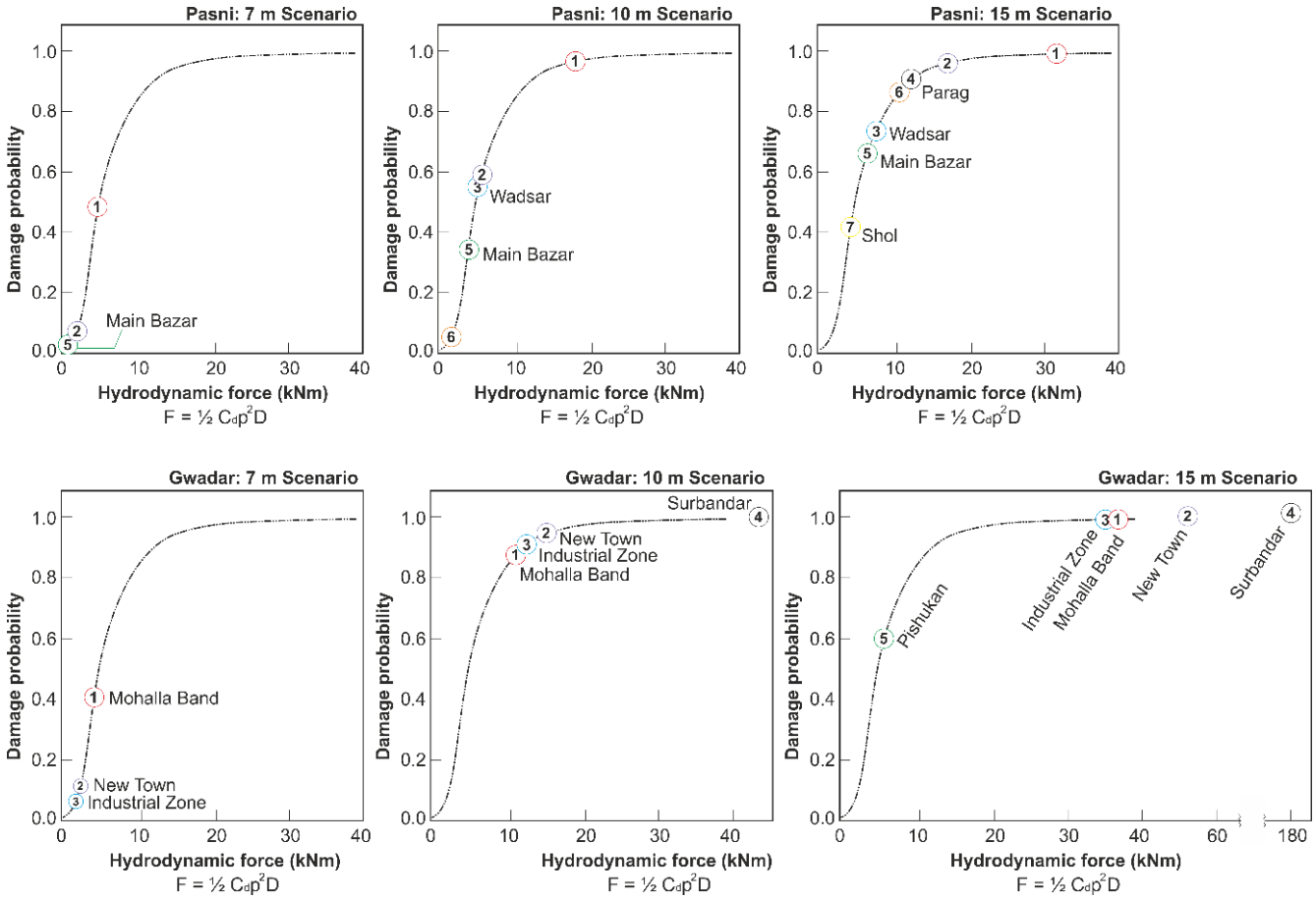

Figure 4: A Probability structural damage plotted against the hydrodynamic force at each monitoring point. Top row: Pasni, Bottom row: Gwadar. The results plotted on fragility curves developed by (Koshimura et al., 2009).